Marine Chemistry 179 (2016) 44–55

Contents lists available at ScienceDirect

Marine Chemistry

journal homepage: www.elsevier.com/locate/marchem

Submarine groundwater discharge in Northern Monterey Bay, California: Evaluation by mixing and mass balance models

Alanna L. Lecher [a,*], Andrew T. Fisher [a], Adina Paytan [b]

[a] Department of Earth and Planetary Sciences, University of California Santa Cruz, Santa Cruz, CA 95064, United States
[b] Institute of Marine Sciences, University of California Santa Cruz, Santa Cruz, CA 95064, United States

ARTICLE INFO

Article history:
Received 28 July 2015
Received in revised form 19 January 2016
Accepted 20 January 2016
Available online 26 January 2016

Keywords:
Submarine groundwater discharge
Radium
Nutrients
Coastal

ABSTRACT

Monterey Bay, California (CA) receives nutrients from multiple sources, including river discharge, upwelling of deep water, and submarine groundwater discharge (SGD). Here we evaluate the relative importance of these sources to Northern Monterey Bay with a mixing model that integrates radium isotopes (^{224}Ra, ^{223}Ra, ^{228}Ra) and nutrient concentrations (SiO_4, NO_3, and PO_4). We also apply a radium isotope based mass balance model to determine SGD and associated nutrient fluxes to Monterey Bay at four sites. Our findings indicate that SGD is a relatively consistent source of nutrients across locations and seasons to Northern Monterey Bay, with fluid input on the order of 10–50 L min^{-1} m^{-1} of coastline, and the greatest impact of SGD fluxes is close to shore. In contrast, nutrient inputs from rivers and upwelling are more variable spatially and temporally. SGD nutrient fluxes are lower where seawater intrusion into coastal aquifers may limit flow of nutrient-rich meteoric groundwater into the coastal ocean.

1. Introduction

Submarine groundwater discharge (SGD) can be an important source of nutrients and other groundwater constituents to coastal ecosystems across the globe, particularly in areas where runoff, rivers, and other nutrient sources are minimal (Shellenbarger et al., 2006; Street et al., 2008; Kroeger and Charette, 2008; Knee and Paytan, 2011). SGD can be fresh meteoric groundwater or seawater that has entered the coastal aquifer through tide and wave action and is subsequently discharged back to the ocean (Knee and Paytan, 2011; Moore, 2006). In California (CA), SGD has been found to range from 6 to 43 L min^{-1} m^{-1} of shore at Stinson Beach, 4 to 9 L min^{-1} m^{-1} of shore at Huntington Beach, and <1 to 21 L min^{-1} m^{-1} of shore in San Francisco Bay (Boehm et al., 2006; de Sieyes et al., 2011; Null et al., 2012). In these locations, SGD is a source of nutrients to the coastal ocean water, although its importance relative to other nutrient sources is unclear. Most of the SGD at these sites is re-circulated seawater (Boehm et al., 2006; de Sieyes et al., 2011; Null et al., 2012).

No previous studies have evaluated the role of SGD as a source of nutrients to large open bays with natural nutrient inputs from upwelling processes, typical of Eastern Boundary Current Systems. We address this gap by quantifying the influence that SGD has on nutrient loading at a site where other nutrient sources to the coastal ocean (upwelling, deep mixing, rivers, runoff) are prevalent and well-studied. We use a mixing model to determine the area of influence of SGD and other nutrient sources to the coastal ocean, and a mass balance model to determine the nutrient loads from SGD.

Monterey Bay, CA lies within a national marine sanctuary and is characterized by a strong seasonal cycle with respect to nutrient and water sources. The major nutrient sources to Northern Monterey Bay (NMB) are upwelling of deep nutrient-rich water, deep mixing, river discharge, and runoff that is largely entrained in rivers (Breaker and Broenkow, 1994; Pennington and Chavez, 2000). Upwelling around NMB, which is largely governed by the intensity of off-shore winds, is strongest from March to August (Graham and Largier, 1997). However, the input of deep water in Monterey Canyon (central Monterey Bay) is more complex and can occur anytime of the year (Shea and Broenkow, 1982). The rainy season in Monterey Bay typically extends from October to April, and largely governs river flow into NMB, although a small amount of base flow (groundwater discharge to streams) may occur year round (Hanson, 2003). During the late summer many rivers that discharge into the NMB develop berms at their mouths, limiting exchange between the rivers and the bay. A companion study of one coastal site in NMB showed that SGD contributes to the nutrient load in this area throughout the year, and that nutrient loading through SGD can overcome nutrient limitation, increasing phytoplankton growth (Lecher et al., 2015b). Here we employ naturally occurring tracers to calculate the SGD flux at multiple sites in NMB using mixing and mass balance models; we also compare this flux to other nutrient sources to the surface water of the bay during different seasons.

Radium (Ra) has four commonly used isotopes, ^{224}Ra, ^{223}Ra, ^{228}Ra, and ^{226}Ra, with half-lives of 3.5 days, 11.5 days, 5.7 years, and 1600 years, respectively. Radium concentration is measured by way of

* Corresponding author.
E-mail address: alecher@ucsc.edu (A.L. Lecher).

http://dx.doi.org/10.1016/j.marchem.2016.01.001
0304-4203/

its decay to daughter isotopes. Therefore it is most commonly denoted by units of activity, disintegrations per minute (dpm) or Becquerels (Bq), per some volume of water. Brackish and saline groundwater are enriched in radium relative to seawater. River water, particularly if fed by groundwater base flow, can also be enriched compared to seawater (Moore and Krest, 2004). The enrichment is the result of interactions between groundwater and the aquifer substrate, in which radium is generated from the decay of parent isotopes and ultimately the origin isotopes of their decay series (^{238}U for ^{226}Ra, ^{232}Th for ^{228}Ra and ^{224}Ra, and ^{235}U for ^{223}Ra). This radium enrichment of brackish and saline groundwater makes radium a good natural tracer for submarine groundwater discharge (Moore, 1999).

2. Methods

2.1. Study site

Four sites in and around NMB were chosen for sampling as part of this study (Fig. 1). Three of the sites (listed in order north to south) Seabright Beach (SB, 36° 57.796′ N, 122° 0.524′ W), Rio Del Mar Beach (RDM, 36° 58.049′ N, 121° 54.291′ W), and Sunset Beach (SS, 36° 52.790′ N, 121° 49.685′ W) were located within NMB, whereas Salinas River Beach (SA, 36° 47.460′ N, 121° 47.594′ W) is located at the mouth of Elkhorn Slough, just south of NMB. Streams discharge into NMB near three of the study sites. The San Lorenzo River discharges into Monterey Bay at SB, Aptos Creek discharges at RDM, and Elkhorn Slough, which is connected to Carneros Creek, discharges ~1 km north of SA.

2.2. General sampling methods

Discrete seawater, groundwater, and river water samples were collected at each site, at the end of the wet season, herein referred to as "spring" (April–June 2012), and at the end of the dry season, herein referred to as "fall" (September–October 2012). Groundwater (which from here on refers to the fluid drawn from the coastal aquifer, the beach face where meteoric groundwater and re-circulated seawater mix) samples were collected from freshly dug pits or temporary PVC well points of a depth < 3 m. Near shore seawater (surf zone) and river water samples were collected by wading. Seawater samples were also collected along transects extending from shore to a common point at the mouth of Monterey Bay (Fig. 1). Ten seawater samples were collected from the surface, and another ten seawater samples were taken from 13–18 m below the surface (generally thought to be below the thermocline) from each transect (Kudela and Chavez, 2000; Ryan et al., 2008). Salinity and temperature were recorded with a YSI hand-held Pro30.

2.3. Radium activity

Large volume (80–120 L) seawater and river water samples were collected using either submersible pumps or buckets, whereas groundwater samples (volume 13–120 L) were collected using submersible pumps. Sample water was passed through a plastic column containing MnO_2-coated acrylic fiber at a rate of <2 L min^{-1} for the collection of Ra isotopes (Moore, 1976). Samples were analyzed at the University of California Santa Cruz on a Radium Delayed Coincidence Counter

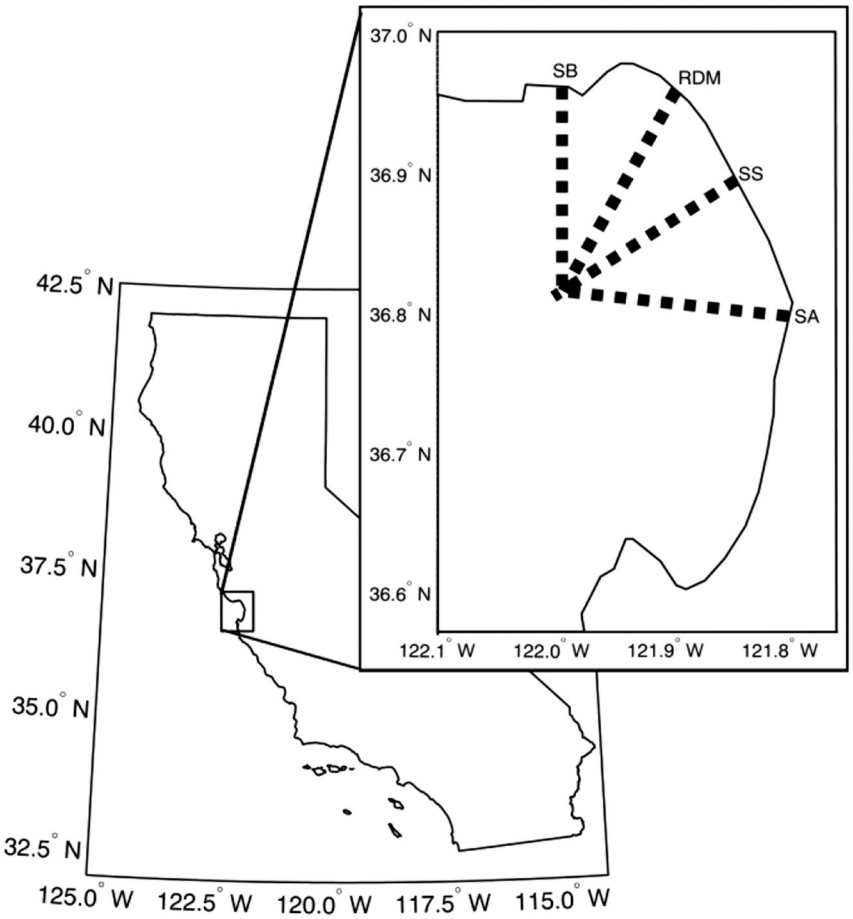

Fig. 1. A map of the transects and associated beaches in Monterey Bay.

(RaDeCC) for the measurement of ^{223}Ra and ^{224}Ra activities within 3 days (Moore and Arnold, 1996; Moore, 2008). The fibers were analyzed on the RaDeCC again 3–5 weeks after the collection for ^{228}Th ingrowth and correction of ^{224}Ra. Fibers were run on the RaDeCC 1.5 years after the collection for ^{228}Ra via the measurement of ^{224}Ra, a decay product (Moore, 2008; Young et al., 2008). Standards were run on the RaDeCC monthly for efficiency calculation and analytical errors were calculated using established methods (Garcia-Solsona et al., 2008).

2.4. Nutrient concentrations

Nutrient samples were collected contemporaneously with radium samples. Samples were collected in 500 mL acid-cleaned (HCl) HPDE bottles by submersible pump or by submerging the collection bottle in the ocean, river, or groundwater well. Within 24 h of collection, samples were filtered through 0.45 μm filter and frozen until analysis. Samples were analyzed at Oregon State University on a Flow Injection Auto Analyzer (Lachat Instruments Model QuickChem 8000).

2.5. SGD fluxes

SGD fluxes were calculated at each site (following the box model of Lecher et al., 2015a, based originally on Hwang et al., 2005) for steady state flows:

$$^{223}_{G}RaSGD + {}^{223}_{R}RaR = {}^{223}_{B}Ra\lambda_{223} + {}^{223}_{E}Ra/\tau \quad (1)$$

$$^{224}_{G}RaSGD + {}^{224}_{R}RaR = {}^{224}_{B}Ra\lambda_{224} + {}^{224}_{E}Ra/\tau \quad (2)$$

$$^{228}_{G}RaSGD + {}^{228}_{R}RaR = {}^{228}_{B}Ra\lambda_{228} + {}^{228}_{E}Ra/\tau \quad (3)$$

$^{224}_{G}Ra$, $^{223}_{G}Ra$, $^{228}_{G}Ra$, $^{224}_{R}Ra$, $^{223}_{R}Ra$, and $^{228}_{R}Ra$ represent the activities (dpm 100 L^{-1}) in groundwater (of the coastal aquifer) and river water of each isotope. $^{223}_{B}Ra$, $^{224}_{B}Ra$, and $^{228}_{B}Ra$ represent the total activity (dpm) in the coastal box for each isotope. $^{223}_{E}Ra$, $^{224}_{E}Ra$, and $^{228}_{E}Ra$ represent the excess (above background) activity (dpm) in each box for each isotope. λ_{223}, λ_{224}, and λ_{228} represent the decay constants (day^{-1}) of each isotope, and τ represents the residence time (days) of water in the box at that site. We assume that steady state conditions apply for each sampling period, 2–3 days for each transect, based on the observation that groundwater levels, ocean current conditions, and tide magnitude do not change much over each sampling period or even each season in which sampling occurred (i.e. spring or fall), and the depth of the mixed layer to be 4 m as has been previously established (Hanson, 2003; Kudela and Chavez, 2000; Ryan et al., 2008).

SGD and *R* represent the volume fluxes of SGD and river water to each box (at each site). The flux within each box is normalized to 1 m of shoreline. While *SGD* is assumed to directly discharge into the box, *R* represents the flux of river water to that segment of shoreline, either directly or from currents carrying river water from another section of shoreline. Thus *R* is the contribution of river water to the box, not river discharge. SGD fluxes were calculated at each site using site-specific groundwater and river water radium activities, except for SS, where the activities of the Salinas River were used for the river water, as the Salinas River discharges nearest to SS. The distance that each box extends from shore was determined by excess radium activity. Total radium activity of the box at each site was determined by fitting a curve to the radium activity (y-axis) of each isotope vs. distance from shore (x-axis) and integrating the equation.

Eqs. (1) to (3) were rearranged to isolate unknown terms and generate a matrix equation of the form $Ax = b$ where A is observed radium activities in the groundwater, river water, and each ocean box, x is a vector of unknown terms (*SGD*, *R*, and τ), and b is a vector of known terms (the product of activity and the radioactive decay constant of radium isotopes in each ocean box).

To fill the matrix A and vector b, the distributions of the ocean and groundwater data sets for each site were determined using the chi-squared test for continuous distributions ($\alpha = 0.05$) against uniform, Gaussian, log-normal, and exponential distributions. We used the distribution of each data set and a pseudo-random number generator to create 10^6 artificial data sets and solve for the unknown vector x. Non-real solutions were avoided by adding negative signs to sink terms in matrix A, and forcing positive solutions using nonnegative least-squares approach (Lawson and Hanson, 1995). Results for vector x were aggregated, median values were computed for discharge, and standard error of model runs were computed to estimate error. This method of modeling end-member distributions and calculating results for many synthetic data sets drawn from these distributions avoids having to assign a single value for each end member (e.g., end-member median or mean), allowing us to estimate the uncertainty in the mixing terms (Knee et al., 2011).

2.6. Mixing model

We used a linear mixing model (following Moore, 2003; Moore et al., 2006; Young et al., 2008) to ascertain the relative contribution of different nutrient source waters to the surface waters of NMB. End member source waters were defined as groundwater (representing the SGD end-member of the coastal aquifer), deep (sub-thermocline) water, river water, and surficial ocean water advected from elsewhere:

$$^{224}_{G}Ra\varphi + {}^{224}_{D}Ra\varepsilon + {}^{224}_{R}Ra\zeta = {}^{R224}_{I}Ra \quad (4)$$

$$^{223}_{G}Ra\varphi + {}^{223}_{D}Ra\varepsilon + {}^{223}_{R}Ra\zeta = {}^{R223}_{I}Ra \quad (5)$$

$$^{228}_{G}Ra\varphi + {}^{228}_{D}Ra\varepsilon + {}^{228}_{R}Ra\zeta = {}^{R228}_{I}Ra \quad (6)$$

$$S_G\varphi + S_D\varepsilon + S_R\zeta = S_I \quad (7)$$

$$N_G\varphi + N_D\varepsilon + N_R\zeta = N_I \quad (8)$$

$$P_G\varphi + P_D\varepsilon + P_R\zeta = P_I \quad (9)$$

$$\omega + \varphi + \varepsilon + \zeta = 1 \quad (10)$$

φ, ε, and ζ represent the fractions of groundwater, deep water, river water, and advected surface ocean water at each surface sampling location (the unknowns) in each transect respectively. $^{224}_{X}Ra$, $^{223}_{X}Ra$, $^{228}_{X}Ra$, are radium activities (dpm 100 L^{-1}), S_X, N_X, and P_X are SiO_4, NO_3, and PO_4 concentrations (μmol L^{-1}), and $X = G$ for groundwater, D for deep water, R for river water, and I for NMB surface water at each point in each transect. Eqs. (4)–(9) were solved simultaneously for each of the 10 sampling locations for each transect (Fig. 1), plus the near shore surf zone, with an algorithm that ensures non-negative solutions (Lawson and Hanson, 1995). Then Eq. (10) was solved to determine the fraction of surficial ocean water advected from elsewhere, which has unknown radium activities and nutrient concentrations. Statistical significance was determined between the end-member constituent activities/concentrations using ANOVA. Only consistently significant constituents were used in the mixing model.

3. Results

3.1. Transect observations

Box plots of observed radium activity and nutrient concentrations in groundwater, deep ocean water, river water, and surficial ocean water are shown for all sites in Fig. 2. Radium activities are highest in groundwater, followed by river water, then surface ocean water, and lowest in

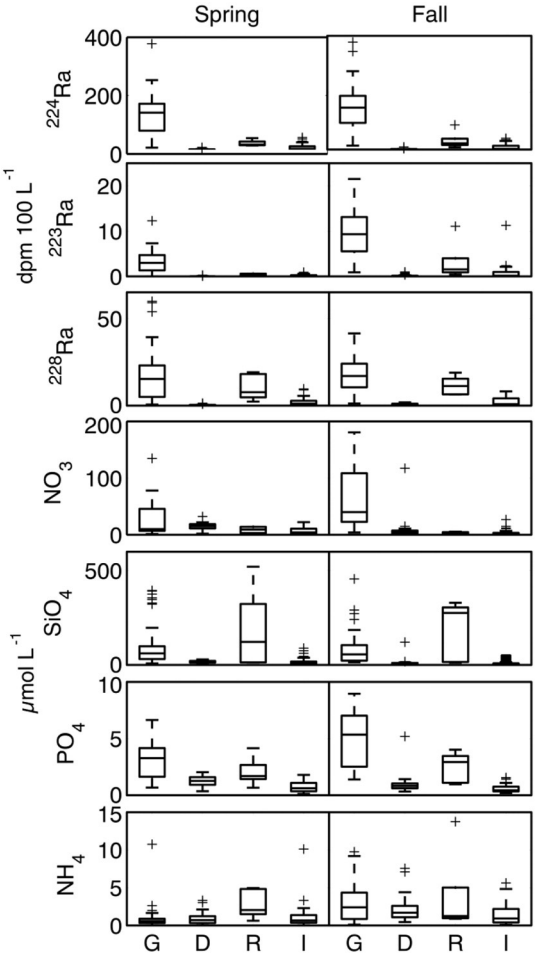

Fig. 2. Box plots of ^{224}Ra, ^{223}Ra, and ^{228}Ra activities and NO_3, SiO_4, PO_4, and NH_4 concentrations in groundwater (G), river water (R), surficial ocean water (I) and deep water (D) for all transects combined, for the spring (left column) and fall (right column). Units for radium are in dpm 100 L^{-1} and for nutrients in μmol L^{-1}. The central line is the median, edges of the box are the 25th and 75th percentiles, whiskers extend to outermost non-outlier data points, and x's are outliers. Differences between end members of ^{224}Ra, ^{223}Ra, and ^{228}Ra activities and NO_3, SiO_4, and PO_4 concentrations are statistically significant, while differences between NH_4 end-member concentrations are not.

deep water. NO_3 concentrations are also highest in groundwater, followed by deep water, then river water, and lowest in surface ocean water. SiO_4 concentrations are highest in river water, followed by groundwater, deep water, and finally surface ocean water. PO_4 concentrations are highest in groundwater, then river water, then deep water, and then surface ocean water.

These trends are consistent in both the spring and the fall, and the differences between each end-member and surficial ocean water are statistically significant using ANOVA (Table 1). Large F-values indicate the variability between the means for each sample type (groundwater, river water, surface water, deep water) in each season (Fig. 2) is high relative to the variability within each sample type (e.g. within all groundwater samples) for each season. *p*-Values are a measure of the probability that the means of each sample type are the same. Small *p*-values ($p < 0.01$) indicate that the difference in the means for each sample type is highly significant. The ANOVA results of all radium isotope activities and NO_3, SiO_4, and PO_4 concentrations for both seasons have extremely small *p*-values (Table 1); hence each solute's end-member averages are significantly different. NH_4 concentrations are similar across all sample types for each season, and the ANOVA results show $p > 0.01$, indicating differences in NH_4 concentrations of the end-members are not statistically significant. For this reason, NH_4 is not used in the mixing model and is not further discussed.

Table 1
F-value and *p*-value of ANOVA of groundwater, surficial ocean water, river water, and deep water end-members.

Constituent	Spring		Fall	
	F-value	Prob > F *p*-Value	F-value	Prob > F *p*-Value
^{224}Ra	76.03	$\leq 2.18 \times 10^{-5}$	77.80	$\leq 1.87 \times 10^{-5}$
^{223}Ra	15.72	$\leq 6.85 \times 10^{-5}$	65.91	$\leq 7.78 \times 10^{-5}$
^{228}Ra	22.86	$\leq 6.45 \times 10^{-5}$	57.54	$\leq 4.67 \times 10^{-5}$
NO_3	4.21	6.90×10^{-3}	31.86	$\leq 2.01 \times 10^{-5}$
SiO_4	19.65	$\leq 1.11 \times 10^{-5}$	25.02	$\leq 1.10 \times 10^{-5}$
PO_4	5.26	1.80×10^{-3}	82.89	$\leq 9.10 \times 10^{-5}$
NH_4	0.92	0.43	3.16	0.03

Radium activities and NO_3, SiO_4, and PO_4 concentrations plotted against distance from shore for the spring and fall for each transect show distinct spatial trends (Fig. 3a). Radium activities are similar in pattern for all isotopes and during both seasons, being the highest close to shore (~30 dpm 100 L^{-1} for ^{224}Ra, 0.25–2 dpm 100 L^{-1} for ^{223}Ra, and ~5 dpm 100 L^{-1} for ^{228}Ra) then decreasing to background levels (near zero) by 5 km from shore. ^{228}Ra activities remain elevated above background levels beyond 5 km, as do ^{223}Ra activities for the SS transect.

Patterns in nutrient concentrations with distance from shore vary by transect and season. NO_3 concentrations are elevated at the shore (~10 μmol L^{-1}) for both seasons. NO_3 concentrations decrease along steep gradients to 0–5 μmol L^{-1} within 1–5 km from shore. In the spring, NO_3 concentrations increase again after 5 km to ~20 μmol L^{-1}. SiO_4 concentrations are also elevated near shore in both seasons, but SiO_4 concentrations are higher in the spring (up to 45 μmol L^{-1}) than in the fall (up to 20 μmol L^{-1}). The highest concentrations of SiO_4 near shore are from sites close to rivers. In the spring SiO_4 concentrations reach a minimum (near zero) at 1–5 km from shore, but increase again (up to 20 μmol L^{-1}) beyond 5 km from shore, similar to NO_3 concentrations. In the fall, SiO_4 concentrations decrease beyond 1 km to 0–10 μmol L^{-1}, where concentrations remain for most of the rest of the transect. PO_4 concentrations are elevated (0.5–1.5 μmol L^{-1}) close to shore only at transects near rivers. PO_4 concentrations reach a near zero minimum for all transects between 0–5 km from shore before increasing again up to 2 μmol L^{-1} offshore.

Temperature and salinity transects show seasonal variations (Fig. 3b). In the spring temperature decreases with distance from shore with a range of 14–16 °C in the near shore and 10–12 °C of shore. Temperature also decreases with distance from shore in the fall, but is about 1 °C warmer close to shore, and follows a shallower temperature gradient than in the spring. Salinity in the spring is more variable than temperature. The near shore of SB and RDM have the lowest salinity of all ocean values at 30–31, whereas the rest of the sampling points have higher salinity (32–33.5). Salinity in the fall for all transects is similar both among sites and within each transect (32.5–33.5). Sites having lower salinity near shore in the spring also tend to have higher SiO_4 concentrations (Fig. 3a).

3.2. SGD fluxes

Box plots of groundwater ^{224}Ra, ^{223}Ra, and ^{228}Ra activities and NO_3, SiO_4, and PO_4 concentrations at each site are shown in Fig. 4. ^{224}Ra medians (93–160 dpm 100 L^{-1}) are similar across all sites in both seasons except for SA in the fall, which has a median of 272 dpm 100 L^{-1}, and is statistically different from all other groundwater activities (ANOVA, Tukey–Kramer, $p < 0.05$). Groundwater ^{223}Ra in the spring shows medians of 2–6 dpm 100 L^{-1}, with a slight trend (not statistically significant) of increasing activity in the southern sites. In the fall ^{223}Ra groundwater activities have higher medians (6–14 dpm 100 L^{-1}) and the SA activities are significantly higher than the other sites. ^{228}Ra

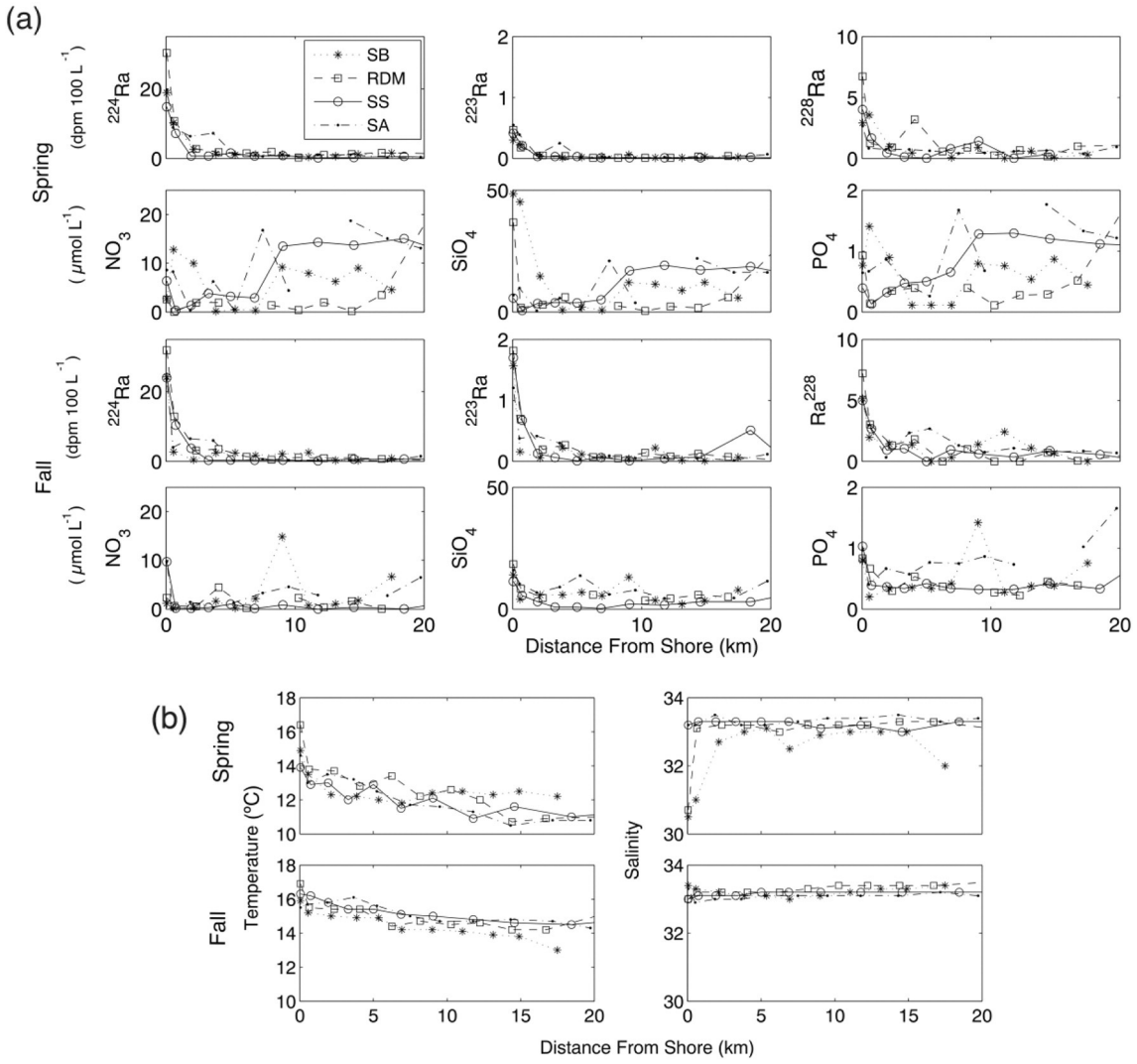

Fig. 3. (a) Radium activities (dpm 100 L^{-1}) and nutrient concentrations (μmol L^{-1}) with distance from shore (km) for each transect for the spring (top two rows) and fall (bottom two rows). (b) Temperature (°C, left column) and salinity (right column) with distance from shore (km) for each transect for the spring (top row) and fall (bottom row).

medians show a greater range of activities in the fall (4–25 dpm 100 L^{-1}) than in the spring (13–18 dpm 100 L^{-1}), but the differences are not statistically significant.

Groundwater NO_3 concentrations are lower in the spring (6–40 μmol L^{-1}) than in the fall (16–145 μmol L^{-1}), with the highest values (spring RDM, SB and SS) being statistically different from their fall counterparts. Median groundwater SiO_4 concentrations are also generally lower in the spring (11–94 μmol L^{-1}) than in the fall (15–106 μmol L^{-1}), and SB and RDM are statistically higher than the other sites in both seasons. PO_4 median groundwater concentrations like the other nutrients are lower in the spring (2–5 μmol L^{-1}) than in the fall (2–7 μmol L^{-1}). However only spring values at RDM are statistically different. All nutrient and radium groundwater end-members were normally distributed as per the chi-squared test.

To determine the ${}^{223}_{B}Ra$, ${}^{224}_{B}Ra$, and ${}^{228}_{B}Ra$ (total activity of the boxes in Eqs. (1)–(3)) a trend line was fitted to the distribution of ^{224}Ra, ^{223}Ra, and ^{228}Ra with distance from shore (similar to Fig. 3, but with background radium activities subtracted). Equations of the trend lines and their fits are shown in Table 2. All of the equations are of exponential decay form Se^{-ix}, where S is the radium activity in the surf zone (for example, 128–195 dpm m^3 for ^{224}Ra), x is the distance from shore in m, and i is a constant determined by how radium concentration decreases with distance from shore. Equations in Table 2 were numerically integrated between limits of 0 to 6000 (0 to 6 km from shore) to represent the area where excess radium is observed (defined by where curve intersects x-axis), and ${}^{223}_{B}Ra$, ${}^{224}_{B}Ra$, and ${}^{228}_{B}Ra$ calculated. ${}^{223}_{G}Ra$, ${}^{224}_{G}Ra$, ${}^{228}_{G}Ra$, ${}^{223}_{R}Ra$, ${}^{224}_{R}Ra$, and ${}^{228}_{R}Ra$ were determined using numerical techniques based on the data distributions, as described in the methods.

Results (SGD fluxes, residence times, and river fluxes) of the mass balance model are shown in Fig. 5. Error bars represent the standard deviation of all model results. SGD fluxes (left column) in the spring (top row) were similar at SB, RDM, and SA (8.9 ± 0.2, 9.8 ± 0.1, and 13 ± 1 L min^{-1}), with a substantially higher flux at SS (48 ± 4 L min^{-1}). In the fall (bottom row), SS also displays the highest flux, slightly higher than in the spring (54.8 ± 0.1 L min^{-1}). SB and RDM SGD fluxes are also higher in the fall (18.42 ± 0.04 L min^{-1} and 33.3 ± 0.1 L min^{-1}, respectively), but SA SGD fluxes are lower in the fall (1.39 ± 0.8 L min^{-1}).

Residence times (middle column) of water in the boxes (the area of excess radium activity, within 6 km of shore) show a wide range (2–179 days) across the sites and seasons. Residence times of water within the SB, SS, and SA boxes in the spring (top row) are similar (24 ± 1, 35 ± 1, and 22 ± 1 days), whereas the residence time of RDM is nearly three times as long (114 ± 1 days). In the fall, (bottom row) SA again has the shortest residence time (2 ± 1 days), whereas SS has the longest residence time (179 ± 1 days), and SB and RDM falling in between (90 ± 1 days and 45 ± 1 days). Residence times represent snapshots of physical conditions at each transect, indicating

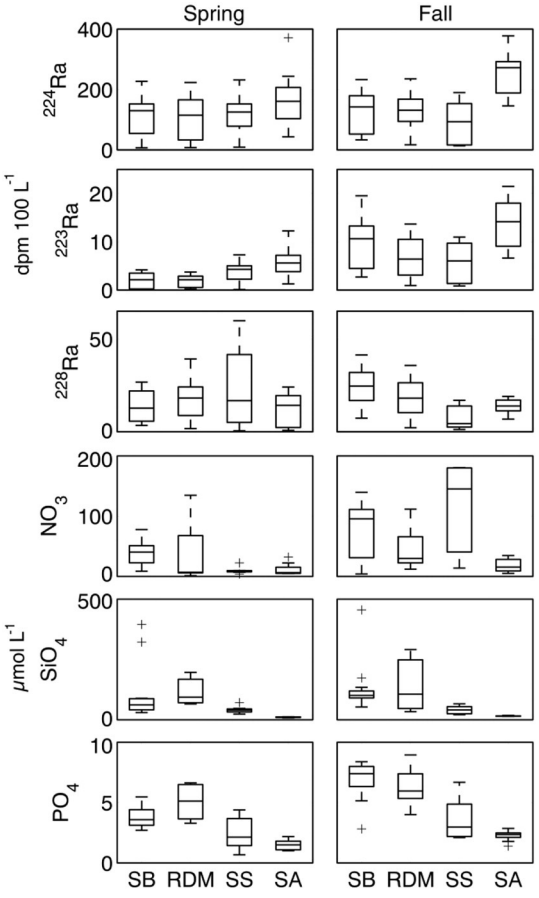

Fig. 4. Box plots of ^{224}Ra, ^{223}Ra, and ^{228}Ra activities and NO_3, SiO_4, and PO_4 concentrations in groundwater for each beach SB, RDM, SS, and SA, for the spring (left column) and fall (right column). Units for radium are in dpm 100 L^{-1} and for nutrients in μmol L^{-1}.

how quickly circulation and water exchange occurred when samples were collected.

In the spring river water contributions to each box (normalized to 1 m of shoreline) are similar at SB and RDM (146 ± 7 L m^{-1} min^{-1}), higher at SS (222 ± 6 L m^{-1} min^{-1}), and lower at SA (86 ± 3 L m^{-1} min^{-1}). In the fall, river contributions at SB, RDM, and SS are minimal (0 ± 3 L m^{-1} min^{-1}). In the fall SA displays the highest river contribution of all calculated at 503 ± 1 L m^{-1} min^{-1}.

Table 2
Best-fit equations and r^2 values of the fit for ^{224}Ra, ^{223}Ra, and ^{228}Ra for each transect, for each season in Fig. 3.

	Spring		Fall	
Isotope	Equation	r^2	Equation	r^2
SB				
^{224}Ra	$137e^{-6E-4x}$	0.93	$153e^{-0.002x}$	0.89
^{223}Ra	$2.36e^{-6E-4x}$	0.81	$8.56e^{-0.001x}$	0.77
^{228}Ra	$34.9e^{-6E-4x}$	0.97	$66.3e^{-9E-4x}$	0.71
RDM				
^{224}Ra	$160e^{-5E-4x}$	0.82	$193e^{-5E-4x}$	0.85
^{223}Ra	$3.13e^{-6E-4x}$	0.94	$11.3e^{-4E-4x}$	0.84
^{228}Ra	$33.8e^{-5E-4x}$	0.71	$95.4e^{-9E-4x}$	0.78
SS				
^{224}Ra	$128e^{-7E-4x}$	0.95	$195e^{-9E-4x}$	0.89
^{223}Ra	$2.44e^{-5E-4x}$	0.94	$14.6e^{-0.001x}$	0.98
^{228}Ra	$92.9e^{-0.002x}$	0.81	$77.7e^{-0.001x}$	0.83
SA				
^{224}Ra	$162e^{-4E-4x}$	0.78	$167e^{-7E-4x}$	0.66
^{223}Ra	$4.53e^{-5E-4x}$	0.94	$9.57e^{-5E-4x}$	0.79
^{228}Ra	$14.6e^{-3E-4x}$	0.45	$58.1e^{-0.002x}$	0.99

SGD-associated nutrient fluxes (normalized to 1 m of shoreline, Fig. 6) were calculated by multiplying the NO_3, SiO_4, and PO_4 average groundwater concentrations at each site (bottom three rows in Fig. 4) by the corresponding SGD volume fluxes (first column Fig. 5). NO_3 fluxes (top row) for the spring (left column) are similar across all sites (0.5–1 mol m^{-1} day^{-1}). In the fall (right column), SA NO_3 fluxes are similar to the spring (<1 mol m^{-1} day^{-1}), but are higher at SB and RDM (2 mol m^{-1} day^{-1} at both) and SS (9 mol m^{-1} day^{-1}). SGD-associated SiO_4 fluxes (middle row) in the spring are similar for SB and RDM (1–2 mol m^{-1} day^{-1}), lowest at SA (0.2 mol m^{-1} day^{-1}), and highest at SS (2.5 mol m^{-1} day^{-1}). SiO_4 fluxes in the fall are generally lower than in the spring, with the lowest flux at SA, as in the spring. SS has the next lowest SiO_4 flux (0.5 mol m^{-1} day^{-1}), followed by SB (0.8 mol m^{-1} day^{-1}), and the highest at RDM (almost 2 mol m^{-1} day^{-1}). SGD-associated PO_4 fluxes (bottom row) are generally lower than NO_3 and SiO_4 fluxes. In the spring (left column) SA and SB have similarly low fluxes (0.05 mol m^{-1} day^{-1}) and RDM and SS have higher fluxes (0.2 mol m^{-1} day^{-1}). In the fall, SA has the lowest PO_4 flux (less than 0.05 mol m^{-1} day^{-1}), RDM and SS have the highest fluxes (~0.3 mol m^{-1} day^{-1}), and SB falls between the others (0.2 mol m^{-1} day^{-1}).

3.3. Mixing model

End-member values for the mixing model equations (left hand side Eqs. (4)–(9)) were taken from the mean of data in Fig. 2, and the Monterey Bay surface water values (right hand side Eqs. (4)–(9)) were taken from the data obtained at each location (Fig. 3a). Results of the mixing model show the relative fractions of groundwater, river water, and deep water present in the surface ocean at each sampling point in each transect (Fig. 7a). Here again, groundwater refers to groundwater collected from the beach face with salinities ranging from 0.1 to 33.9 in the spring and 2 to 34.2 in the fall. The contribution of surficial ocean water advected into the transect area (calculated with Eq. (10)), is the largest component at many points, but is not shown to make the other trends easier to see (fractions of all end-members are shown in SI Fig. 2). To test the robustness of the model in the spring, the mixing model was also run using the end-member medians (slightly lower than the means), generating similar results in terms of the relative proportions of end member mixing (SI Fig. 1).

The contribution of groundwater to all transects (in both seasons) is the highest close to shore (10–25%). This relative contribution decreases along a steep gradient with distance from shore, with no contribution beyond 10 km. The contribution of deep water (by upwelling, deep mixing, or any other mechanism) across all sites is greater in the spring (up to 100%) than in the fall (up to 40%). In the spring, deep water contribution generally increases with distance from shore (within our sampling area). This is most robust in the RDM and SS transects where the deep water contribution close to shore is 0% but increases to 100% beyond 10 km. The SA and SB transects show more complex trends in the spring, with deep water influence in patches both in the near shore (<5 km) and offshore (>5 km). In the fall, deep water influence is smallest along the SB transect, with most of the transect showing no influence and one point (~9 km from shore) showing 10–20% deep water contributions. The SS transect shows a greater influence of deep water with most of the sampling beyond 7 km showing a contribution of about 10%. RDM and SA transects are similar in the fall in that they show minimal contribution of deep water to the near shore, but offshore contributions of 20–40%.

Aggregated transect model results show a distinct seasonal trend (Fig. 7b). Groundwater in both seasons displays the highest influence close to shore (10–25%), with the contribution reduced to essentially 0% at distances ≥5 km. Despite larger variability between transects, the deep water contribution in both seasons increases with distance from shore. Deep water contribution is greater in the fall (up to 100%)

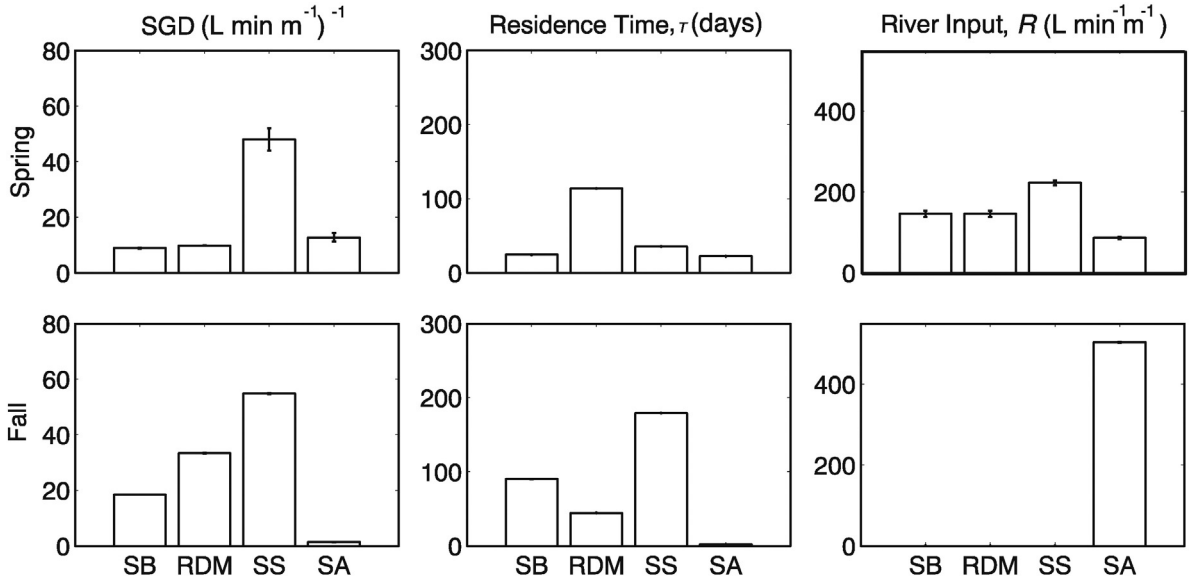

Fig. 5. Box model results for each site for the spring (top row) and the fall (bottom row). SGD and river input are in L min^{-1} m^{-1}. Advection is in days.

than in the spring when it does not surpass 25%. River water contribution is minimal in the average plots across both transects and seasons.

4. Discussion

The box model calculations (Fig. 5) provide estimates of both the volume flux of SGD to the coastal ocean and the residence time of surface water in different parts of NMB. SGD volume fluxes at all study sites are of the same order of magnitude (10–60 L min^{-1} m^{-1}) with the exception of SA in the fall, which has a much lower flow rate (~5 L min^{-1} m^{-1}). SGD volume fluxes at SS are the greatest and are similar across the seasons (~60 L min^{-1} m^{-1}). This range is similar to calculated SGD fluxes (<1–43 L min^{-1} m^{-1}) at other beaches in California with similar geology and oceanographic conditions as mentioned in the introduction (Boehm et al., 2006; de Sieyes et al., 2011; Null et al., 2012).

The water mass residence times at different locations in the bay are important because rapid exchange and mixing (shorter residence time) will diminish the impact of land-based nutrient loads, whereas longer residence times may allow greater accumulation and internal processing (uptake, transformation). Previous studies have suggested that there are areas of entrainment (long residence time) within parts of Monterey Bay at certain times of the year (Mackey et al., 2012; Ryan et al., 2008, 2009). Our box model calculations suggest a longer residence time in the SS area in the fall (~200 days) compared to the spring (~50 days), perhaps indicative of stratification and pooling. While such a long residence time may seem unrealistic for the natural system, these results are characteristic of conditions at the times and locations of sampling. This means that these calculated residence times could result if there were persistent conditions as observed (wind strength and direction, current strength and direction, presence of an upwelling event or river flush). As wind and currents change day to day, apparent residence times based on these methods would change.

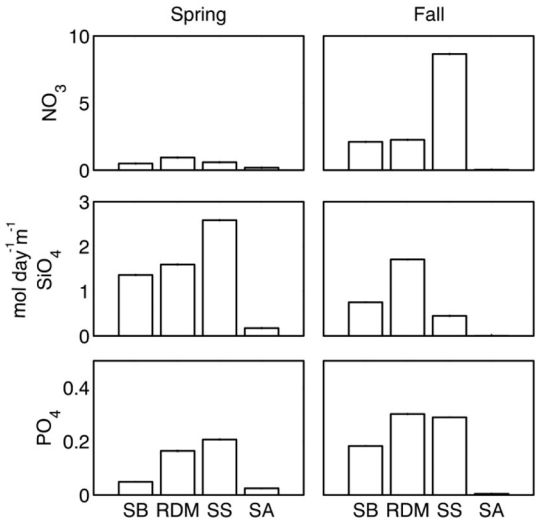

Fig. 6. SGD-associated NO_3 (top row), SiO_4 (middle row), and PO_4 (bottom row) fluxes at each site for the spring (left column) and fall (right column). Units are in mol day^{-1} m^{-1}.

RDM is located north of SS, and the box model suggests a shorter residence time at RDM in the fall (~50 days) compared to that at SS (~200 days). RDM was sampled the week prior to SS, and the pooling of water may not have occurred at RDM yet, leading to a shorter calculated residence time than would have been detected had sampling occurred in the following week at SS. The SGD flux at RDM is higher in the fall (~35 L min^{-1}) than in the spring (~10 L min^{-1}). The combined effect of this increase in SGD volume flux with the shorter residence time in the fall (~50 days) compared to the spring (~120 days), may lead to a similar influence of SGD across the seasons at RDM.

Previous studies have calculated an average residence time of 6 days in the near shore (4 km–30 m in these studies) of Monterey Bay using heat, nutrient concentrations, and freshwater replacement methods (Broenkow and Smethie, 1978; Graham and Largier, 1997). These studies calculated residence times for a much smaller area (as small as 30 m from shore, compared to 6 km from shore in the present paper), and used different tracers (heat and nutrients). Radium offers advantages as a tracer for residence time because it has only two main sinks, advection and radioactive decay. Omission of additional sources and/or sinks in earlier studies could lead to longer calculated residence times (Broenkow and Smethie, 1978). In addition, earlier studies focused on locations to the periphery of our study area, at the mouth of the San Lorenzo River (SB) and Elkhorn Slough (SA), which is where our shortest calculated residence times are 24 days at SB (in the spring) and 2 days at SA (in the fall). Thus our results overlap with the results from earlier studies, but suggest that longer residence times are more typical for NMB.

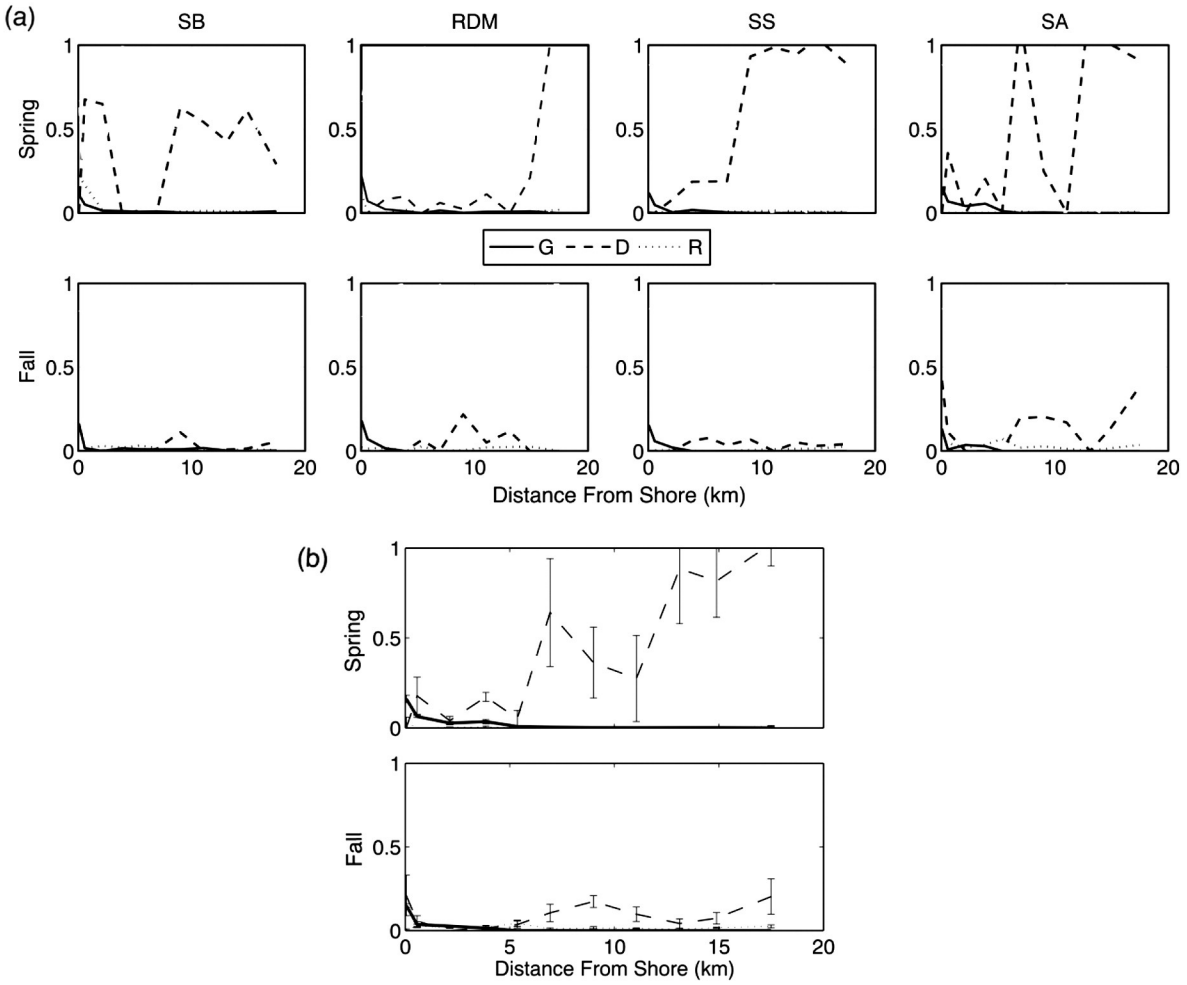

Fig. 7. (a) Mixing model results for the spring (top row) and fall (bottom row) for each of the transects SB (first column), RDM (second column), SS (third column), and SA (fourth column). Y-axis represents the fraction of the water type at that point in the transect (G, groundwater; R, river water; D, deep water). X-axis is the distance from shore in km. (b) Average of mixing model results transect for the spring (top row) and fall (bottom row). Error bars represent the standard error of transect results.

While not directly accounted for in the mass balance model, large volume fluxes of deep water into the bay would shorten apparent residence times. Comparing the spring residence times of the transects calculated from the mass balance model (Fig. 5), when deep water fluxes are the greatest (Fig. 7), it is apparent that shorter residence times in the SB, SS, and SA transects coincide greater deep water contributions. The longest spring residence time (the RDM transect) coincides with the least amount of deep-water influence. It is gratifying that these two calculations are consistent, as they were completed independently on the basis of separate data sets.

The influence of SGD on NMB is also regulated by the concentration of nutrients in groundwater and therein the SGD-associated nutrient flux. We use the average nutrient concentration at each site, which spanned salinities from 0.1 to 34.2, as the end-member nutrient concentrations for the nutrient flux calculation. Since radium data used as input for the SGD flux model were collected contemporaneously with samples that generated nutrient data, these data represent the same type of groundwater (a mix of meteoric groundwater and recirculated seawater) and mean values were used to represent the groundwater end-member.

Nutrient concentrations at each site span several orders of magnitude (Fig. 4), suggesting that end member concentrations of SGD are more important than SGD fluid flow rates (the latter being relatively constant) in influencing nutrient delivery. For example, the SGD volume flux at SS is the same in the fall and the spring (Fig. 5), whereas the NO_3 flux (Fig. 6) is substantially lower in the spring (1 mol m^{-1} day^{-1}) than in the fall (9 mol m^{-1} day^{-1}). Substantially higher NO_3 fluxes in the fall than in the spring are also seen in SB, RDM, and SS. SiO_4 fluxes are more similar across sites, generally falling in the 0.5–2.4 mol m^{-1} day^{-1} range, except for SA which is <0.2 mol m^{-1} day^{-1} across both seasons. The differences in variability between NO_3 fluxes (highly variable) and SiO_4 fluxes (less variable) lie in the nature of the two nutrients, specifically their sources in groundwater and the processes that affect their concentration in the aquifer and SGD during transport.

To ascertain the processes that influence nutrient concentrations in the coastal aquifer, we compare NO_3, SiO_4, and PO_4 concentrations to salinity for each season within the coastal aquifer (Fig. 8). Unlike NO_3, SiO_4 only has one source in the coastal aquifer: the dissolution of aquifer rock. Low salinity samples have high SiO_4 concentrations, whereas high salinity samples have low SiO_4 concentrations, with all other samples falling between the two end-members. This conservative mixing relationship shows how high SiO_4 concentration groundwater is diluted by low concentration SiO_4 water close to shore in the coastal aquifer (heavily seawater influenced). This can be seen especially well in the fall and spring in SB and RDM, and SS in the fall, where there are strong salinity gradients. This trend is not so clearly seen in SS spring and SA fall and spring, where all groundwater collected was saline and of a similarly low SiO_4 concentrations.

Contrary to SiO_4, NO_3 and PO_4 concentrations do not show evidence for conservative mixing. NO_3 and PO_4 have many sources in the coastal aquifer (landfill, septic systems, and agriculture). The proximity and connectivity of these sources to the coastal aquifer and the fact that

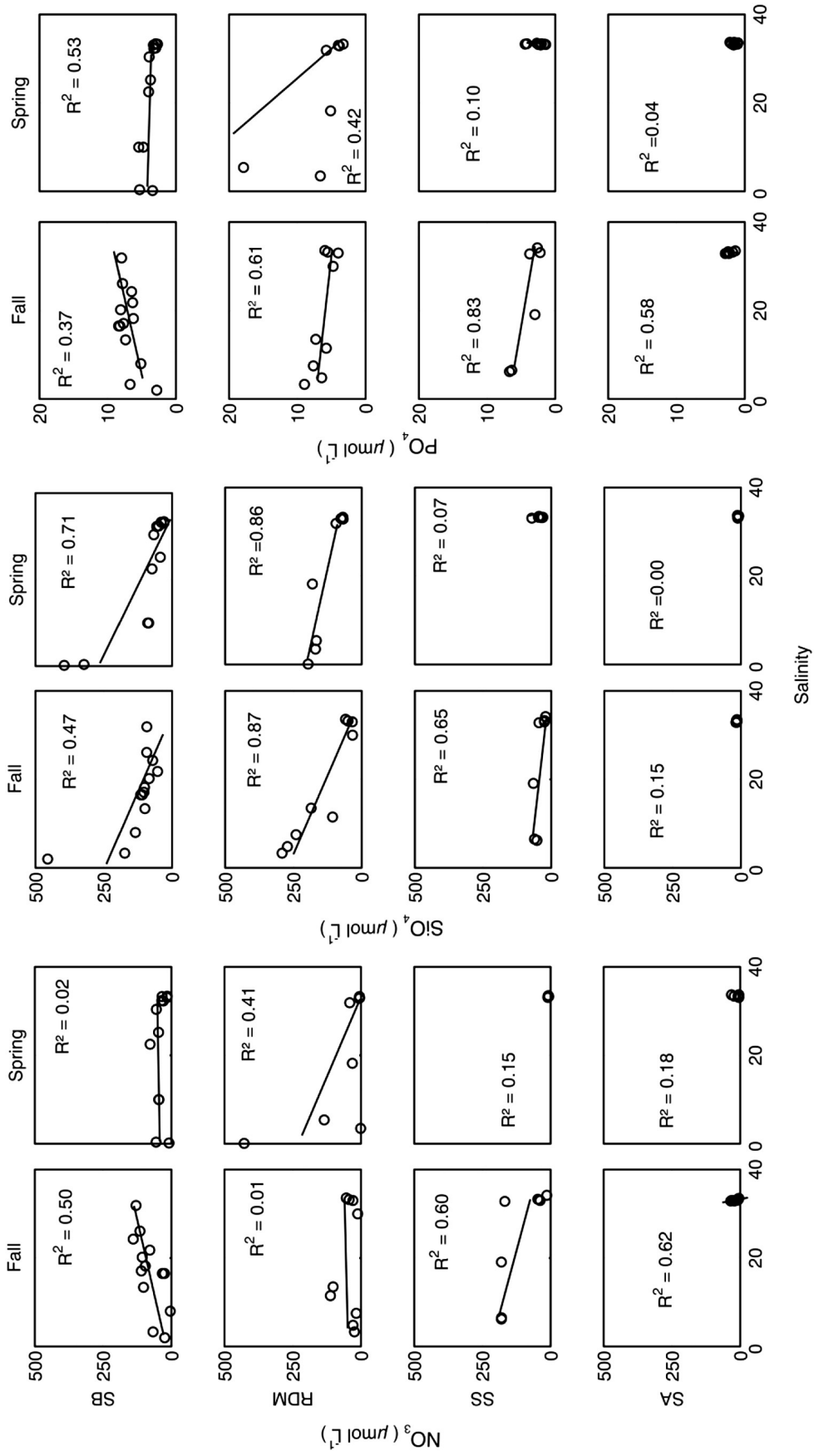

Fig. 8. Coastal aquifer NO_3 (left two columns), SiO_4 (middle two columns), and PO_4 (right two columns) vs. salinity (X-axis) for SB (top row), RDM (second row), SS (third row), and SA (bottom row) for the fall (left column of each pair) and the spring (right column of each pair). Units for nutrients are in μmol L^{-1}.

NO_3 and PO_4 can undergo chemical transformations in the coastal aquifer, make their concentrations more heterogeneous across seasons and sites (Kroeger and Charette, 2008; Slomp and Van Cappellen, 2004). Proximity to NO_3 sources (inland) within the coastal aquifer is shown by the high NO_3 concentrations paired with low salinity, which can be seen in SS in the fall and RDM in the spring. In the fall at SB, NO_3 concentrations within the coastal aquifer increase with salinity (closer to the ocean), whereas NO_3 concentrations in the fall at SB are the same across all salinities. PO_4 shows trends similar to those of NO_3 at all of the sites, including increasing concentration with increasing salinity at SB in the spring. These trends suggest that the NO_3 and PO_4 may be coming from the same source, perhaps lateral advection of high nutrient water parallel to shore. Other processes involving the nitrogen cycle that might affect NO_3 concentration (nitrogen-fixation, denitrification) would not affect the PO_4 concentration.

The high salinities observed at SS in the spring and SA in both seasons (Fig. 8) indicate a significant seawater influence and dilution. Unlike all other sites, SA has very low topography, which may contribute to a low hydraulic gradient in the adjacent aquifer and limited meteoric groundwater flow towards the ocean. In addition, there is seawater intrusion in this region as a result of groundwater overdraft, contributing to elevated groundwater salinities several kilometers inland from the coast (Hanson, 2003; Vengosh et al., 2002). SS in the spring similarly has only high-salinity/low-nutrient samples, whereas in the fall at that same site low-salinity/high-nutrient samples were collected. This observation suggests that the hydraulic gradient in the aquifer is important for moving low-salinity/high-nutrient meteoric groundwater to the near shore coastal aquifer, where it mixes with seawater before discharging to the ocean. Indeed, water levels can change on a seasonal time scale at locations in the aquifer near the coast (Hanson, 2003). The SiO_4 concentrations versus salinity plots for SS spring and SA, in both the spring and fall (Fig. 8), also show why NO_3, SiO_4, and PO_4 concentrations (Fig. 4), and therein-calculated fluxes (Fig. 6), are so low. Only high salinity (low concentration) samples were collected on these sampling trips (both seasons of SA and spring SS), indicating that high-salinity groundwater with low-nutrient concentrations dominates SGD.

Beyond calculating SGD and fluxes, and determining the controlling processes of SGD in Monterey Bay, we also compare SGD to other important nutrient sources in the bay, using a mixing model that incorporates three nutrient sources. Mixing model results show that SGD consistently contributes solutes and water across all transects during wet and dry seasons (Fig. 7). Its influence is the highest closest to shore (~20%), and diminishes with distance from shore, reaching a minimum 5–7 km offshore. This is consistent with SGD fluxes being largely decoupled from short-term (seasonal) cycles, and with the dependence of SGD on tidal pumping rather than freshwater gradients close to the aquifer-ocean interface.

Unlike SGD, patterns of nutrient delivery by deep water (sub-thermocline) and river water in NMB (Fig. 7) are more variable than those for SGD. During the spring, when upwelling is most intense, deep water shows a strong influence at all locations, particularly >5 km from shore. There are minima in the deep-water nutrient contributions at some locations farther from shore, likely due to complex circulation patterns. Major points of upwelling during the spring are not located within the bay itself, but are found to the north (Año Nuevo) and the south (Point Sur) (Rosenfeld et al., 1994; Ryan et al., 2009). A large portion of nutrient-rich deep water in Monterey Bay is advected into Monterey Bay from these locations. This is consistent with previous reports that show patchiness of water associated with upwelling in NMB (Rosenfeld et al., 1994). SB and SA also show some influence (20%–70%) of deep water close to shore in the spring, perhaps because of site-specific physiographic conditions. The near shore terminus of SB is near the mouth of Monterey Bay and allows easy access for advected upwelling water from Año Nuevo to the near shore. Almost the entire SA transect overlies the Monterey Canyon, which allows for advection of deep water to the surface of Monterey Bay year round (Shea and Broenkow, 1982; Woodson et al., 2011).

In contrast to the spring, there is little deep water influence in the fall, consistent with there being little contribution from deep water to nutrient budgets along the SB, RDM, and SS transects during this time (Fig. 7). We calculate the strongest deep-water influence along the SA transect in the fall (Fig. 7), consistent with enhanced advection of deep water to the surface above Monterey Canyon. Temperature trends along the transects (Fig. 3b) are consistent with mixing model results, with colder spring temperatures (compared to the fall) being indicative of stronger upwelling (e.g., Graham and Largier, 1997).

Upwelling is a wind driven process most strongly associated with northerly winds. Daily average wind speed and direction at the M2 buoy (http://www.ndbc.noaa.gov/station_history.php?station=46042) at the mouth of Monterey Bay (Fig. 9) show northerly winds (favorable to upwelling) during and preceding the spring sampling, and a general relaxation of wind during and preceding the fall sampling, consistent with our interpretations.

Like deep water and unlike SGD, riverine influence is also highly seasonal in Monterey Bay. River water has little influence on NMB surface water (<10%) for most transects and sites (Fig. 4). Sampling occurred in 2012, which was a hydrologic dry period, with river and creek discharge below historical means. There is somewhat greater river influence near shore at the SB and RDM sites in the spring (Fig. 7), because of inflows from the San Lorenzo River (at SB) and Aptos Creek (at RDM). The San Lorenzo River is the stream with the largest annual and peak discharges in the study area, and both the San Lorenzo River and Aptos Creek discharged very close (within 100 m) to the sampling locations. In contrast, the SS and SA sites are >2 km from the nearest surface discharge sites. Salinity measured along the transects (Fig. 3b) is consistent with mixing model results. Where the mixing model shows the greatest riverine influence, spring SB and RDM in the near shore, ocean salinities are the lowest (30–31), indicating a strong riverine influence in these areas in the spring. Such a low salinity (riverine) signal is absent in the near shore area of these transects in the fall, when the mixing model likewise shows no river influence.

Fall is generally the driest part of the year in NMB, and this is consistent with minimal river influence along all of the transects. However, SA shows more riverine influence in the fall than in the spring in the mixing model, consistent with the mass balance model (503 ± 1 L m^{-1} min^{-1} in the fall and 86 ± 3 L m^{-1} min^{-1} in the spring). While river flows to most of NMB are seasonal, Elkhorn Slough (located near SA) is connected with the ocean via tidal flushing and effectively discharges all year because of harbor dredging. The irrigation-fed Salinas River discharges into the harbor as well, and may account for the presence of more river influence in the fall than in the spring (Black et al., 2009; Wankel et al., 2009), a finding unique to this transect.

Thus it is clear that both deep water and river water, and their associated nutrient contributions to NMB, are strongly seasonal (more influential in the spring than in the fall); unlike SGD, which is influential all year. The difference in the seasonality of deep water and river nutrient fluxes, compared to SGD fluxes, might have been expected, but this is one of the first studies to quantify these relations spatially and temporally across an open ocean setting like NMB.

There are significant limitations to the methods applied and constituents analyzed as part of this study. Nutrients were added to the mixing model along with radium, to better constrain the non-groundwater end-members. For example, SiO_4 concentrations were often highest in river water, making it a valuable tracer of river input. However there are potential errors associated with using biologically reactive constituents in a mixing model that does not include reactions. For example, biological uptake could reduce the concentration of NO_3 in the NMB surface water, resulting in the calculation of a smaller contribution from an end-member NO_3 source. We do not expect biological activity to affect the concentrations of nutrients in the end-members as much as in the surface waters of each NMB transect, because groundwater

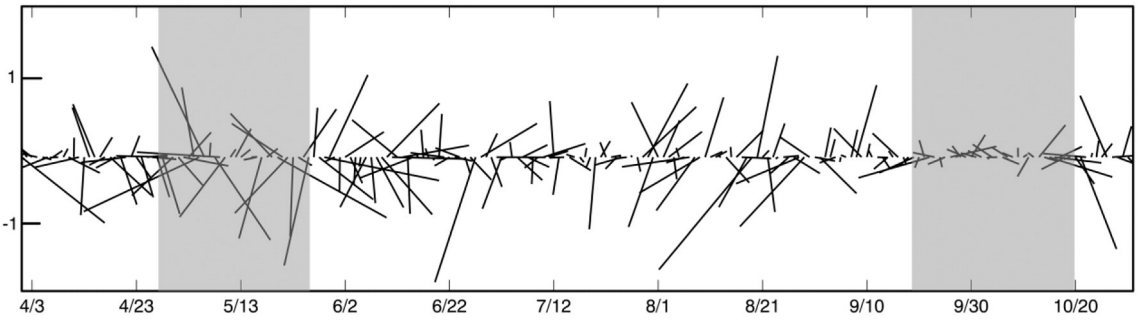

Fig. 9. Daily mean wind speed ($m\ s^{-1}$) for M2 buoy at the mouth of Monterey Bay. Shaded areas correspond to sampling periods. Northerly winds (from the north to the south) are more favorable for upwelling. Other wind directions or relaxed winds typically preclude upwelling.

and deep water are out of the photic zone where most biological activity occurs.

We implemented the mixing model in addition to the box model to portray relative contributions of SGD, river water, and deep water as nutrient sources to the surface water of NMB. The mixing model showed similar results when we used the mean (Fig. 7a) and median (SI Fig. 1) end-member concentrations, and the results are consistent with temperature, salinity and wind data (Figs. 3b and 9). The mixing model incorporates a unity constraint (Eq. (10)) to identify surface water advection, but this term is not otherwise constrained and will incorporate errors in calculations for the other terms. Mixing model results are most useful for considering relative magnitudes, temporal variations, and spatial patterns of input sources, rather than absolute values. The use of biologically reactive constituents is strengthened by simultaneous consideration of non-biologically-reactive radium, and comparison of results to measurements using conservative tracers such as salinity. The data and interpretations presented in this study are specific to the time period of sampling. Hydrologic conditions were relatively dry, greatly reducing the input from coastal streams to NMB. In some ways, this helped to clarify the results, but it could mean that results could be considerably different during more normal to wet conditions.

5. Conclusions

We applied mixing and box models to NMB, based on sampling and measurement of radium and nutrient concentrations, to assess the relative magnitudes of nutrient sources, and to quantify the magnitude of SGD fluxes and water residence times. We find that the influence of SGD in NMB is greatest $\leq$5 km from shore. In contrast, deep water is more important farther from shore. In addition, the apparent magnitude of SGD inflow is relatively consistent across seasons, whereas inputs from other near-shore sources (rivers) and upwelling are highly variable between the seasons. We find that SGD discharges consistently to NMB throughout the year, contributing similar SiO_4 fluxes, but NO_3 and PO_4 fluxes vary both temporally and spatially. Nutrient fluxes are the lowest at sites (e.g. SA) where limited meteoric groundwater discharge (and seawater intrusion) may prevent the transport of high-nutrient groundwater from inland towards the coastal aquifer.

Acknowledgments

This project was funded by the California Sea Grant award 035-CONT-N to AP, ATF, JR and RK, and the UC Water Security and Sustainability Initiative (MR-15-328473) to ATF. We would also like to thank the many undergraduate, graduate, and post-graduate researchers who assisted with the field work. Technical support for small boat sample collection was provided by the UCSC Long Marine Lab.

Appendix A. Supplementary data

Supplementary data to this article can be found online at http://dx.doi.org/10.1016/j.marchem.2016.01.001.

References

Black, F.J., Paytan, A., Knee, K.L., De Sieyes, N.R., Ganguli, P.M., Gray, E., Flegal, a R., 2009. Submarine groundwater discharge of total mercury and monomethylmercury to central California coastal waters. Environ. Sci. Technol. 43, 5652–5659.

Boehm, A.B., Paytan, A., Shellenbarger, G.G., Davis, K.A., 2006. Composition and flux of groundwater from a California beach aquifer: implications for nutrient supply to the surf zone. Cont. Shelf Res. 26, 269–282. http://dx.doi.org/10.1016/j.csr.2005.11.008.

Breaker, L.C., Broenkow, W.W., 1994. The circulation of Monterey Bay and related processes. Oceanogr. Mar. Biol. Annu. Rev. 32, 1–64.

Broenkow, W.W., Smethie, W.M., 1978. Surface circulation and replacement of water in Monterey Bay. Estuar. Coast. Mar. Sci. 6, 583–603. http://dx.doi.org/10.1016/0302-3524(78)90033-6.

de Sieyes, N.R., Yamahara, K.M., Paytan, A., Boehm, A.B., 2011. Submarine groundwater discharge to a high-energy surf zone at Stinson Beach, California, estimated using radium isotopes. Estuar. Coasts 34, 256–268. http://dx.doi.org/10.1007/s12237-010-9305-2.

Garcia-Solsona, E., Garcia-Orellana, J., Masqué, P., Dulaiova, H., 2008. Uncertainties associated with 223Ra and 224Ra measurements in water via a delayed coincidence counter (RaDeCC). Mar. Chem. 109, 198–219. http://dx.doi.org/10.1016/j.marchem.2007.11.006.

Graham, W.M., Largier, J.L., 1997. Upwelling shadows as nearshore retenetion sites: the exampe of northern Monterey Bay. Cont. Shelf Res. 17, 509–532.

Hanson, R., 2003. Geohydrologic Framework of Recharge and Seawater Intrusion in the Pajaro Valley, Santa Cruz and Monterey Counties, California.

Hwang, D.-W., Kim, G., Lee, Y.-W., Yang, H.-S., 2005. Estimating submarine inputs of groundwater and nutrients to a coastal bay using radium isotopes. Mar. Chem. 96, 61–71. http://dx.doi.org/10.1016/j.marchem.2004.11.002.

Knee, K., Paytan, A., 2011. 4.08 submarine groundwater discharge: a source of nutrients, metals, and pollutants to the Coastal Ocean. Treatise Estuar. Coast. Sci. 4, 205–234. http://dx.doi.org/10.1016/B978-0-12-374711-2.00410-1.

Knee, K.L., Garcia-solsona, E., Garcia-orellana, J., Boehm, A.B., Paytan, A., 2011. Oceanography: Methods Using Radium Isotopes to Characterize Water Ages and Coastal Mixing Rates: A Sensitivity Analysis. pp. 380–395.

Kroeger, K.D., Charette, M.a., 2008. Nitrogen biogeochemistry of submarine groundwater discharge. Limnol. Oceanogr. 53, 1025–1039. http://dx.doi.org/10.4319/lo.2008.53.3.1025.

Kudela, R.M., Chavez, F.P., 2000. Modeling the impact of the 1992 El Nino on new production in Monterey Bay, California. Deep Sea Res. Part II 47, 1055–1076. http://dx.doi.org/10.1016/S0967-0645(99)00136-8.

Lawson, C.L., Hanson, R.J., 1995. Solving least squares problems. SIAM Classics in Applied Mathematics http://dx.doi.org/10.2307/2005340.

Lecher, A.L., Kessler, J., Sparrow, K., Garcia-Tigreros Kodovska, F., Dimova, N., Murray, J., Tulaczyk, S., Paytan, A., 2015a. Methane transport through submarine groundwater discharge to the north Pacific and Arctic Ocean at two Alaskan sites. Limnol. Oceanogr. http://dx.doi.org/10.1002/lno.10118.

Lecher, A.L., Mackey, K., Kudela, R., Ryan, J., Fisher, A., Murray, J., Paytan, A., 2015b. Nutrient loading through submarine groundwater discharge and phytoplankton growth in Monterey Bay, CA. Environ. Sci. Technol. http://dx.doi.org/10.1021/acs.est.5b00909 (150519131048004).

Mackey, K.R.M., Mioni, C.E., Ryan, J.P., Paytan, A., 2012. Phosphorus cycling in the red tide incubator region of Monterey Bay in response to upwelling. Front. Microbiol. 3, 33. http://dx.doi.org/10.3389/fmicb.2012.00033.

Moore, W.S., 1976. Sampling ^{228}Ra in the deep ocean. Deep Sea Research and Oceanographic Abstracts 23 (7), 647–651 Elsevier.

Moore, W.S., 1999. The subterranean estuary: a reaction zone of ground water and sea water. Mar. Chem. 65, 111–125. http://dx.doi.org/10.1016/S0304-4203(99)00014-6.

Moore, W.S., 2003. Sources and fluxes of submarine groundwater discharge delineated by radium isotopes. Biogeochemistry 66, 75–93. http://dx.doi.org/10.1023/B:BIOG.0000006065.77764.a0.

Moore, W.S., 2006. The role of submarine groundwater discharge in coastal biogeochemistry. J. Geochem. Explor. 88, 389–393. http://dx.doi.org/10.1016/j.gexplo.2005.08.082.

Moore, W.S., 2008. Fifteen years experience in measuring 224Ra and 223Ra by delayed-coincidence counting. Mar. Chem. 109, 188–197. http://dx.doi.org/10.1016/j.marchem.2007.06.015.

Moore, W., Arnold, R., 1996. Measurement of 223Ra and 224Ra in coastal waters using a delayed coincidence counter. J. Geophys. Res. 101, 1321–1329.

Moore, W.S., Krest, J., 2004. Distribution of 223Ra and 224Ra in the plumes of the Mississippi and Atchafalaya Rivers and the gulf of Mexico. Mar. Chem. 86, 105–119. http://dx.doi.org/10.1016/j.marchem.2003.10.001.

Moore, W.S., Blanton, J.O., Joye, S.B., 2006. Estimates of flushing times, submarine groundwater discharge, and nutrient fluxes to Okatee Estuary, South Carolina. J. Geophys. Res. Ocean 111. http://dx.doi.org/10.1029/2005JC003041.

Null, K.A., Dimova, N.T., Knee, K.L., Esser, B.K., Swarzenski, P.W., Singleton, M.J., Stacey, M., Paytan, A., 2012. Submarine groundwater discharge-derived nutrient loads to San Francisco Bay: implications to future ecosystem changes. Estuar. Coasts 35, 1299–1315. http://dx.doi.org/10.1007/s12237-012-9526-7.

Pennington, J.T., Chavez, F., 2000. Seasonal fluctuations of temperature, salinity, nitrate, chlorophyll and primary production at station H3/M1 over 1989–1996 in Monterey Bay, California. Deep Sea Res. Part II 47, 947–973.

Rosenfeld, L.K., Schwing, F.B., Garfield, N., Tracy, D.E., 1994. Bifurcated flow from an upwelling center: a cold water source for Monterey Bay. Cont. Shelf Res. 14, 931–964. http://dx.doi.org/10.1016/0278-4343(94)90058-2.

Ryan, J.P., Gower, J.F.R., King, S.a., Bissett, W.P., Fischer, A.M., Kudela, R.M., Kolber, Z., Mazzillo, F., Rienecker, E.V., Chavez, F.P., 2008. A coastal ocean extreme bloom incubator. Geophys. Res. Lett. 35, L12602. http://dx.doi.org/10.1029/2008GL034081.

Ryan, J.P., Fischer, A.M., Kudela, R.M., Gower, J.F.R., King, S.a., Marin, R., Chavez, F.P., 2009. Influences of upwelling and downwelling winds on red tide bloom dynamics in Monterey Bay, California. Cont. Shelf Res. 29, 785–795. http://dx.doi.org/10.1016/j.csr.2008.11.006.

Shea, R.E., Broenkow, W.W., 1982. The role of internal tides in the nutrient enrichment of Monterey Bay, California. Estuar. Coast. Shelf Sci. 15, 57–66. http://dx.doi.org/10.1016/0272-7714(82)90036-1.

Shellenbarger, G., Monismith, S., Genin, A., Paytan, A., 2006. The importance of submarine groundwater discharge to the nearshore nutrient supply in the gulf of Aqaba (Israel). Limnology 51, 1876–1886.

Slomp, C.P., Van Cappellen, P., 2004. Nutrient inputs to the coastal ocean through submarine groundwater discharge: controls and potential impact. J. Hydrol. http://dx.doi.org/10.1016/j.jhydrol.2004.02.018.

Street, J.H., Knee, K.L., Grossman, E.E., Paytan, A, 2008. ubmarine groundwater discharge and nutrient addition to the coastal zone and coral reefs of leeward Hawai'i. Mar. Chem. 109 (3), 355–376.

Vengosh, A., Gill, J., Davisson, M.L., Hudson, G.B., 2002. A multi-isotope (B, Sr, O, H, and C) and age dating (H-3-He-3 and C-14) study of groundwater from Salinas Valley, California: hydrochemistry, dynamics, and contamination processes. Water Resour. Res. 38, 1008. http://dx.doi.org/10.1029/2001WR000517.

Wankel, S.D., Kendall, C., Paytan, A., 2009. Using nitrate dual isotopic composition δ15N and (δ18O) as a tool for exploring sources and cycling of nitrate in an estuarine system: Elkhorn Slough, California. J. Geophys. Res. Biogeosci. 114. http://dx.doi.org/10.1029/2008JG000729.

Woodson, C.B., Barth, J.a., Cheriton, O.M., McManus, M.a., Ryan, J.P., Washburn, L., Carden, K.N., Cheng, B.S., Fernandes, J., Garske, L.E., Gouhier, T.C., Haupt, a.J., Honey, K.T., Hubbard, M.F., Iles, a., Kara, L., Lynch, M.C., Mahoney, B., Pfaff, M., Pinsky, M.L., Robart, M.J., Stewart, J.S., Teck, S.J., True, a., 2011. Observations of internal wave packets propagating along-shelf in northern Monterey Bay. Geophys. Res. Lett. 38. http://dx.doi.org/10.1029/2010GL045453 (n/a–n/a).

Young, M.B., Gonneea, M.E., Fong, D.a., Moore, W.S., Herrera-Silveira, J., Paytan, A., 2008. Characterizing sources of groundwater to a tropical coastal lagoon in a karstic area using radium isotopes and water chemistry. Mar. Chem. 109, 377–394. http://dx.doi.org/10.1016/j.marchem.2007.07.010.